Journal of Applied Mathematics and Physics, 2025, 13(5), 1858-1873
https://www.scirp.org/journal/jamp
ISSN Online: 2327-4379
ISSN Print: 2327-4352

Numerical Simulation of Predator-Prey Patterns in Marine Organisms

Shuai Zhang, Zhiyuan Li

Department of Mathematics, Inner Mongolia University of Technology, Hohhot, China
Email: z13784383249@163.com, lizhiyuan2064@126.com

How to cite this paper: Zhang, S. and Li, Z.Y. (2025) Numerical Simulation of Predator-Prey Patterns in Marine Organisms. *Journal of Applied Mathematics and Physics*, **13**, 1858-1873.
https://doi.org/10.4236/jamp.2025.135104

Received: April 22, 2025
Accepted: May 25, 2025
Published: May 28, 2025

Abstract

This paper mainly investigates the application of predator-prey systems. By deriving the first-order principles of the stochastic partial differential equations, we analyzed the stability of the model at the equilibrium point. The coefficients of the outgoing amplitude equation were deduced using the Wakefield nonlinear analysis. The model was numerically simulated by setting parameters using the nine-point difference method, and the simulation results are in agreement with the numerical results. In addition, a marine predator-prey model combining the fear effect and refuge environment is proposed in this paper, and the pattern formation mechanism of species coexistence is revealed through theoretical analysis and numerical simulation.

Keywords

Linear Stability, Nine-Point Difference Method, Weakly Nonlinear Analysis

1. Introduction

The study of marine predator-prey relationships represents a fundamental research focus in marine ecosystems [1], encompassing population dynamics, behavioral ecology, trophic cascades, and climate change impacts. The mathematical foundation for predator-prey dynamics was established by Lotka [2] in 1926 and remains central to theoretical ecology. Arditi [3] advanced this framework by developing a ratio-dependent model that accounts for predation efficiency variations with population density. Roman [4] proposed the whale pump theory, demonstrating through field measurements that marine mammals enhance surface primary productivity by releasing nutrient-rich fecal plumes during vertical migrations, thereby promoting nutrient cycling. Subsequent contributions include Philippe [5] Waswanipi Principle explaining nonlinear dynamics in small pelagic fish-predator systems, Dell [6] findings on temperature-driven metabolic

acceleration in ectothermic predators, and Munday [7] research showing how ocean acidification impairs larval olfactory cue detection. Collectively, these studies reveal that persistent acidification may critically impair sensory functions, reduce population viability, and profoundly impact marine biodiversity.

In natural ecosystems, species interactions [8] and spatial distribution patterns [9] play crucial roles in maintaining ecosystem stability and biodiversity [10]. Recent advances in ecological research have increasingly focused on understanding spatial species distributions and their impacts on population dynamics. Notably, the fear effect [11] and Allee effect [12] have emerged as key factors influencing species distributions and population behaviors, attracting significant research attention. The fear effect characterizes prey psychological and behavioral responses to predator presence [13], while the Allee effect demonstrates how population density affects both the species itself and its predators. These mechanisms critically influence species survival and ecosystem functioning.

This chapter presents a marine predator-prey model incorporating fear effects and refuge environments [14], where prey and predator populations are represented by $X(t)$ and $Y(t)$ respectively. The model introduces a fear factor $F(f_0, Y)$, with f_0 quantifying fear intensity-reflecting how anti-predator behaviors induced by predator presence reduce prey reproduction rates and consequently alter population dynamics. The proposed predator-prey system is formulated as follows:

$$\begin{cases} \dfrac{\mathrm{d}X}{\mathrm{d}t} = \dfrac{aX}{1+f_0 Y}\left(1-\dfrac{X}{K}-\dfrac{m_1}{X+b_1}\right)-\dfrac{c_1(1-e)XY}{(1-e)X+K_1}, \\ \dfrac{\mathrm{d}Y}{\mathrm{d}t} = Y\left(d_1-\dfrac{s_1 Y}{(1-e)X+K_2}\right). \end{cases} \tag{1}$$

In the equations, the fear term $\dfrac{aX}{1+f_0 Y}$ captures observed anti-predator behaviors, such as reduced foraging in damselfish exposed to predator cues. The refuge parameter K_1 quantifies physical protection, analogous to seagrass beds shielding juvenile fish. while $1-\dfrac{X}{K}-\dfrac{m_1}{X+b_1}$ incorporates both the environmental carrying capacity K and Allee effect for the prey population. The term $-\dfrac{c_1(1-e)XY}{(1-e)X+K_1}$ quantifies the predation rate on the prey. The second equation component $\dfrac{s_1 Y}{(1-e)X+K_2}$ describes the predator population dynamics. **Table 1** provides the biological interpretations of all parameters in these equations. To nondimensionalize the system, we introduce the following transformations:

$$u=\frac{X}{K},\ v=\frac{Y}{K},\ t=aT,\ m=\frac{m_1}{K},\ b=\frac{b_1}{K},\ c=\frac{c_1}{a},$$
$$k_1=\frac{K_1}{K},\ K_2=k_1K,\ d=\frac{d_1}{a},\ s_1=ad,\ f=f_0K,$$

Then Equation (1) transforms into:

$$\begin{cases} u_t = \dfrac{u}{1+fv}\left(1-u-\dfrac{m}{u+b}\right)-\dfrac{c(1-e)uv}{(1-e)u+k_1}, \\ v_t = dv\left(1-\dfrac{v}{(1-e)u+k_1}\right). \end{cases} \tag{2}$$

To simulate the spatial dispersal of marine organisms, we incorporate diffusion terms into Equation (2). This modification captures both the predator's prey-tracking behavior and the dynamic relationship between predator velocity and prey diffusion rates [15]. The resulting reaction-diffusion system is formulated as follows:

Table 1. Parameter and Biological significance in the model.

Parameter	Ecological Significance
a	Prey growth rate
K	Environmental carrying capacity for prey species
c_1	Maximum predation rate on prey
K_1	Refuge efficacy: 0.1 - 0.3 for coral reef crevices
m_1	Effect constant
b_1	Effect constant
d_1	Population growth rate of predators
s_1	Predator death rate
K_2	Degree of environmental refuge for predators
f_0	Fear intensity: Measured as 0.3 - 0.6 in lab studies of clownfish

$$\begin{cases} u_t = \dfrac{u}{1+fv}\left(1-u-\dfrac{m}{u+b}\right)-\dfrac{c(1-e)uv}{(1-e)u+k_1}+D_u\nabla^2 u, \\ v_t = dv\left(1-\dfrac{v}{(1-e)u+k_1}\right)+D_v\nabla^2 v. \end{cases} \tag{3}$$

here, ∇^2 represents the Laplacian operator in two-dimensional space. This model incorporates both fear effects and refuge mechanisms, establishing a comprehensive ecological dynamics framework that accurately characterizes spatial predator-prey interactions in natural environments—interactions that directly govern population stability and evolutionary dynamics. Through theoretical analysis of Equation (3), we elucidate the pattern formation mechanisms underlying species coexistence, where marine ecological patterns fundamentally reflect spatial population distributions. These findings not only provide theoretical foundations for interpreting complex ecological phenomena, but also deliver critical scientific support for formulating ecosystem conservation strategies and management policies.

Recent studies have demonstrated that spatial patterns in marine ecosystems, such as phytoplankton blooms and predator hotspots, directly influence nutrient

cycling and species survival. Our model's simulated patterns (e.g., spots and stripes in Figures 1-4) may reflect real-world phenomena like:

1) Prey aggregation in refuge zones (e.g., coral reefs);

2) Predator-driven "fear landscapes" altering prey migration.

2. Linear Stability Analysis

This section investigates the equilibrium solutions of Equation (4) in the absence of diffusion. We consider the following nonlinear system:

$$\begin{cases} f(u,v) = \dfrac{u}{1+fv}\left(1-u-\dfrac{m}{u+b}\right) - \dfrac{c(1-e)uv}{(1-e)u+k_1}, \\ g(u,v) = dv\left(1-\dfrac{v}{(1-e)u+k_1}\right). \end{cases} \tag{4}$$

Analysis reveals that Equation (4) possesses a unique equilibrium point (u_*, v_*), where $v_* = hu_* + k_1$, with u_* given by:

$$u_* = \frac{1-b-ch\left(bfh+\left(fk_1+1\right)\right)+N}{2\left(cfh^2+1\right)}, \tag{5}$$

where, $h = 1-e$,

$$N = \sqrt{\left(b+ch\left(bfh+fk_1+1\right)-1\right)^2 - 4\left(cfh^2+1\right)\left(bch\left(fk_1+1\right)-b+m\right)}.$$

To analyze the stability of the equilibrium point, we first compute the first-order partial derivatives of Equation (4) at the equilibrium:

$$\frac{\partial f}{\partial u} = \frac{1}{1+fv_*}\left(1-2u_*-\frac{mb}{\left(u_*+b\right)^2}\right) - \frac{c(1-e)v_*k_1}{\left((1-e)^2u_*+k_1\right)^2},$$

$$\frac{\partial f}{\partial v} = -\frac{u_*f}{\left(1+fv_*\right)^2}\left(1-u_*-\frac{m}{u_*+b}\right) - \frac{c(1-e)u_*}{(1-e)u_*+k_1},$$

$$\frac{\partial g}{\partial u} = \frac{dv_*^2(1-e)}{\left((1-e)u_*+k_1\right)^2}, \quad \frac{\partial g}{\partial v} = d\left(1-\frac{2v_*}{(1-e)u_*+k_1}\right).$$

The Jacobian matrix of Equation (4) at the equilibrium point (u_*, v_*) is:

$$J = \begin{bmatrix} \dfrac{\partial f}{\partial u} & \dfrac{\partial f}{\partial v} \\ \dfrac{\partial g}{\partial u} & \dfrac{\partial g}{\partial v} \end{bmatrix}, \tag{6}$$

The characteristic equation corresponding to Equation (4) at the equilibrium point:

$$\lambda^2 - Tr_0\lambda + Det_0 = 0, \tag{7}$$

where, Tr_0 denotes the trace of the Jacobian matrix J, and Det_0 represents the determinant of the Jacobian matrix J.

$$Tr_0 = \frac{\partial f}{\partial u} + \frac{\partial g}{\partial v}, \quad Det_0 = \frac{\partial f}{\partial u}\frac{\partial g}{\partial v} - \frac{\partial g}{\partial u}\frac{\partial f}{\partial v}.$$

According to the Routh-Hurwitz stability criterion [16], we obtain Table 2. The stability analysis in Table 2 demonstrates that the equilibrium point is locally asymptotically stable when $Tr_0 < 0$ and $Det_0 > 0$.

Table 2. Judgment of stability.

Trace of a matrix (Tr)	Determinant of a matrix (Δ)	$Tr^2 - 4\Delta$	Stability
$Tr < 0$	$\Delta > 0$	$Tr^2 - 4\Delta < 0$	Stable
$Tr = 0$	$\Delta > 0$	$Tr^2 - 4\Delta < 0$	Stable
$Tr > 0$	$\Delta > 0$	$Tr^2 - 4\Delta > 0$	Unstable
$Tr = 0$	$\Delta > 0$	$Tr^2 - 4\Delta > 0$	Unstable
$\forall Tr$	$\Delta < 0$	$\forall\left(Tr^2 - 4\Delta\right)$	Unstable

3. Weakly Nonlinear Analysis

Above, we analyze the dynamical behavior of fractional non-diffusive ordinary differential equations. In this section, we will reveal various spatiotemporal behaviors around the Turing bifurcation threshold d and derive the amplitude equations associated with the Equation (3) using multiscale and weakly nonlinear analytical methods.

Apply a perturbation to the equilibrium point E^*, such that $u = \tilde{u}^* + \tilde{u}$, $v = \tilde{v}^* + \tilde{v}$, and bringing them into Equation (3) and performing a Taylor expansion, yields

$$\begin{cases} \dfrac{\partial \tilde{u}}{\partial t} = \tilde{D}_u \nabla^2 \tilde{u} + \tilde{a}_{11}\tilde{u} + \tilde{a}_{12}\tilde{v} + \tilde{c}_{20}\tilde{u}^2 + \tilde{c}_{02}\tilde{v}^2 + \tilde{c}_{11}\tilde{u}\tilde{v} \\ \qquad + \tilde{c}_{30}\tilde{u}^3 + \tilde{c}_{03}\tilde{v}^3 + \tilde{c}_{21}\tilde{u}^2\tilde{v} + \tilde{c}_{12}\tilde{u}\tilde{v}^2, \\ \dfrac{\partial \tilde{v}}{\partial t} = \tilde{D}_v \nabla^2 \tilde{u} + \tilde{a}_{11}\tilde{u} + \tilde{a}_{22}\tilde{v} + \tilde{d}_{20}\tilde{u}^2 + \tilde{d}_{02}\tilde{v}^2 + \tilde{d}_{11}\tilde{u}\tilde{v} \\ \qquad + \tilde{d}_{30}\tilde{u}^3 + \tilde{d}_{03}\tilde{v}^3 + \tilde{d}_{21}\tilde{u}^2\tilde{v} + \tilde{d}_{12}\tilde{u}\tilde{v}^2, \end{cases} \tag{8}$$

where

$$c_{11} = \frac{c(e-1)}{k - u(e-1)} + \frac{f\left(u + \dfrac{m}{b+u} - 1\right)}{(fv+1)^2} + \frac{cu(e-1)^2}{\left(k - u(e-1)\right)^2} - \frac{fu\left(\dfrac{m}{(b+u)^2} - 1\right)}{(fv+1)^2},$$

$$c_{20} = \frac{2\left(\dfrac{m}{(b+u)^2} - 1\right)}{fv+1} + \frac{2cv(e-1)^2}{\left(k_1 - u(e-1)\right)^2} - \frac{2mu}{(b+u)^3(fv+1)} + \frac{2cuv(e-1)^3}{\left(k_1 - u(e-1)\right)^3},$$

$$c_{02} = -\frac{2f^2 u\left(u + \dfrac{m}{b+u} - 1\right)}{(fv+1)^3}, \quad c_{12} = \frac{2f^2 u\left(\dfrac{m}{(b+u)^2} - 1\right)}{(fv+1)^3} - \frac{2f^2\left(u + \dfrac{m}{b+u} - 1\right)}{(fv+1)^3},$$

$$c_{21}=\frac{2c(e-1)^2}{(k_1-u(e-1))^2}-\frac{2f\left(\frac{m}{(b+u)^2}-1\right)}{(fv+1)^2}+\frac{2cu(e-1)^3}{(k_1-u(e-1))^3}+\frac{2fmu}{(b+u)^3(fv+1)^2},$$

$$c_{30}=\frac{6cv(e-1)^3}{(k_1-u(e-1))^3}-\frac{6m}{(b+u)^3(fv+1)}+\frac{6mu}{(b+u)^4(fv+1)}+\frac{6cuv(e-1)^4}{(k_1-u(e-1))^4},$$

$$c_{03}=\frac{6f^3u\left(u+\frac{m}{b+u}-1\right)}{(fv+1)^4},\ d_{11}=-\frac{2dv^2(e-1)^2}{(k_1-u(e-1))^3},\ d_{20}=-\frac{2dv^2(e-1)^2}{(k_1-u(e-1))^3},$$

$$d_{02}=-\frac{2d}{k_1-u(e-1)},\ d_{12}=-\frac{2d(e-1)}{(k_1-u(e-1))^2},\ d_{21}=-\frac{4dv(e-1)^2}{(k_1-u(e-1))^3},$$

$$d_{30}=-\frac{6dv^2(e-1)^3}{(k_1-u(e-1))^4},\ d_{03}=0.$$

For facilitate writing, $\tilde{u}$, $\tilde{v}$ will still be recorded as u, v below. Let $U=(u,v)^{\mathrm{T}}$, Equation (8) can be simplified as

$$\frac{\partial U}{\partial t}=JU+M(U,U), \tag{9}$$

$$J=\begin{pmatrix}a_{11}+D_u\nabla^2u & a_{12}\\ a_{21} & a_{22}+D_v\nabla^2v\end{pmatrix},$$

where

$$M=\begin{pmatrix}c_{20}\tilde{u}^2+c_{02}\tilde{v}^2+c_{11}\tilde{u}\tilde{v}+c_{30}\tilde{u}^3+c_{03}\tilde{v}^3+c_{21}\tilde{u}^2\tilde{v}+c_{12}\tilde{u}\tilde{v}^2\\ d_{20}\tilde{u}^2+d_{02}\tilde{v}^2+d_{11}\tilde{u}\tilde{v}+d_{30}\tilde{u}^3+d_{03}\tilde{v}^3+d_{21}\tilde{u}^2\tilde{v}+d_{12}\tilde{u}\tilde{v}^2\end{pmatrix}+\mathcal{O}(4),$$

where L denotes a linear operator, N represents a nonlinear operator.

Subsequently, by expanding the parameter b, the solution U and the nonlinear term N, with a sufficiently small parameter ϵ, we obtain:

$$b_c-b=\epsilon b_1+\epsilon^2b_2+\epsilon^3b_3+\mathcal{O}(\epsilon^3). \tag{10}$$

Develop the variable U and the nonlinear term N in relation to this minor parameter:

$$U=\begin{pmatrix}u\\ v\end{pmatrix}=\epsilon\begin{pmatrix}u_1\\ v_1\end{pmatrix}+\epsilon^2\begin{pmatrix}u_2\\ v_2\end{pmatrix}+\epsilon^3\begin{pmatrix}u_3\\ v_3\end{pmatrix}+\mathcal{O}(\epsilon^3), \tag{11}$$

$$M=\epsilon^2M_2+\epsilon^3M_3+\mathcal{O}(\epsilon^4), \tag{12}$$

where

$$M_2=\begin{pmatrix}k_{20}u_1^2+k_{11}u_1v_1\\ m_{20}u_1^2+m_{11}u_1v_1\end{pmatrix},$$

$$M_3=\begin{pmatrix}2k_{20}u_1u_2+k_{11}u_1v_2+k_{11}u_2v_1+k_{30}u_1^3+k_{21}u_1^2v_1\\ 2m_{20}u_1u_2+m_{11}u_1v_2+m_{11}u_2v_1+m_{30}u_1^3+m_{21}u_1^2v_1\end{pmatrix}.$$

Decompose operator L into the following form:

$$J = J_c + (b - b_T) N,$$

where

$$J_c = \begin{pmatrix} D_u \nabla^2 u + a_{11}^* & a_{12}^* \\ a_{21}^* & D_v \nabla^2 v + a_{22}^* \end{pmatrix}, \ a_{ij}^* = a_{ij}(\mu_T),$$

$$N = \begin{pmatrix} b_{11} & b_{12} \\ b_{21} & b_{22} \end{pmatrix}.$$

Using the multiple-scale approach, we obtain the 1st order of $(\mathcal{O}(\epsilon))$:

$$J_c \begin{pmatrix} u_1 \\ v_1 \end{pmatrix} = 0. \tag{13}$$

The solution of the Equation (13) is

$$\begin{pmatrix} u_1 \\ v_1 \end{pmatrix} = \begin{pmatrix} \phi \\ 1 \end{pmatrix} \sum_{j=1}^{3} \left(W_j e^{i \boldsymbol{q}_j \cdot r} \right) + c.c., \tag{14}$$

where $\phi = \dfrac{-a_{12}^*}{a_{11}^* - D_u q_c^2}, \left| \boldsymbol{q}_j \right| = q_c, q_c = q_T(\gamma_T)$. Additionally, Z_j denotes the amplitude associated with the mode of $e^{i \boldsymbol{q}_j \cdot r}$.

The 2^{nd} order of $(\mathcal{O}(\epsilon^2))$:

$$J_c \begin{pmatrix} u_2 \\ v_2 \end{pmatrix} = \frac{\partial}{\partial S_1} \begin{pmatrix} u_1 \\ v_1 \end{pmatrix} - b_1 N \begin{pmatrix} u_1 \\ v_1 \end{pmatrix} - M_2 = \begin{pmatrix} F_u \\ F_v \end{pmatrix}, \tag{15}$$

F_u^j and $F_v^j (j = 1,2,3)$ are the coefficients with respect to $e^{i \boldsymbol{q}_j \cdot r}$ in F_u and F_v respectively.

In line with the Fredholm solvability condition, for Equation (15) to possess a nontrivial solution, the vector function on the right-hand side must be perpendicular to the zero eigenvalue of L_c^+. The zero eigenvector of L_c is:

$$\begin{pmatrix} 1 \\ \beta \end{pmatrix} e^{-i q_j r} + c.c., \ \ j = 1,2,3, \tag{16}$$

with $\beta = -\dfrac{a_{11}^* - D_u q_c^2}{a_{21}^*}$. From the orthogonal condition:

$$(1, \beta) \begin{pmatrix} F_u^j \\ F_v^j \end{pmatrix} = 0, \ \ j = 1,2,3. \tag{17}$$

Utilizing the Fredholm solvability condition as stated in (17), we arrive at the following:

$$\begin{cases} (\phi + \beta) \dfrac{\partial Z_1}{\partial S_1} = b_1 g_0 Z_1 + 2(k_1 + \beta h_2) \bar{Z}_2 \bar{Z}_3, \\ (\phi + \beta) \dfrac{\partial Z_2}{\partial S_1} = b_1 g_0 Z_2 + 2(k_1 + \beta h_2) \bar{Z}_1 \bar{Z}_3, \\ (\phi + \beta) \dfrac{\partial Z_3}{\partial S_1} = b_1 g_0 Z_3 + 2(k_1 + \beta h_2) \bar{Z}_1 \bar{Z}_2, \end{cases} \tag{18}$$

where

$$\begin{cases} g_0 = (\phi b_{11} + b_{22}) + \beta(\phi b_{21} + b_{22}), \\ g_1 = \dfrac{1}{2} c_{20}\phi^2 + c_{11}\phi, \\ g_2 = \dfrac{1}{2} d_{20}\phi^2 + d_{11}\phi. \end{cases}$$

Next, higher-order disturbance terms are introduced:

$$\begin{aligned} \begin{pmatrix} u_2 \\ v_2 \end{pmatrix} = \begin{pmatrix} U_0 \\ V_0 \end{pmatrix} + \sum_{j=1}^{3} \begin{pmatrix} U_j \\ V_j \end{pmatrix} \mathrm{e}^{i\boldsymbol{q}_j \cdot r} + \sum_{j=1}^{3} \begin{pmatrix} U_{jj} \\ V_{jj} \end{pmatrix} \mathrm{e}^{2i\boldsymbol{q}_j \cdot r} + \begin{pmatrix} U_{12} \\ V_{12} \end{pmatrix} \mathrm{e}^{i(\boldsymbol{q}_1 - \boldsymbol{q}_2)\cdot r} \\ + \begin{pmatrix} U_{23} \\ V_{23} \end{pmatrix} \mathrm{e}^{i(\boldsymbol{q}_2 - \boldsymbol{q}_3)\cdot r} + \begin{pmatrix} U_{31} \\ V_{31} \end{pmatrix} \mathrm{e}^{i(\boldsymbol{q}_3 - \boldsymbol{q}_1)\cdot r} + c.c., \end{aligned} \tag{19}$$

From the orthogonal condition, we obtain:

$$\begin{cases} (\phi+\beta)\left(\dfrac{\partial X_1}{\partial S_1} + \dfrac{\partial Z_1}{\partial S_2}\right) = g_0(b_2 Z_1 + b_1 X_1) + 2(g_1 + \beta g_2)\left(\overline{Z_2 X_3} + \overline{Z_3 X_2}\right) \\ \qquad - \left[(P_1 + \beta T_1)|Z_1|^2 + (P_2 + \beta T_2)\left(|Z_2|^2 + |Z_3|^2\right)\right] Z_1, \\ (\phi+\beta)\left(\dfrac{\partial X_2}{\partial S_1} + \dfrac{\partial Z_2}{\partial S_2}\right) = g_0(b_2 Z_2 + b_1 X_2) + 2(g_1 + \beta g_2)\left(\overline{Z_1 X_3} + \overline{Z_3 X_1}\right) \\ \qquad - \left[(P_1 + \beta T_1)|Z_2|^2 + (P_2 + \beta T_2)\left(|Z_1|^2 + |Z_3|^2\right)\right] Z_2, \\ (\phi+\beta)\left(\dfrac{\partial X_3}{\partial S_1} + \dfrac{\partial Z_3}{\partial S_2}\right) = g_0(b_2 Z_3 + b_1 X_3) + 2(g_1 + \beta g_2)\left(\overline{Z_2 X_1} + \overline{Z_1 X_2}\right) \\ \qquad - \left[(P_1 + \beta T_1)|Z_3|^2 + (P_2 + \beta T_2)\left(|Z_2|^2 + |Z_1|^2\right)\right] Z_3, \end{cases}$$

where

$$P_1 = -(2\phi c_{02} + c_{11})(u_{00} + u_{11}) - \phi c_{11}(v_{00} + v_{11}) - 3c_{12}\phi^2,$$

$$P_2 = -(2\phi c_{02} + c_{11})(u_{00} + u_*) - \phi c_{11}(v_{00} + v_*) - 6c_{12}\phi^2,$$

$$T_1 = -(2\phi d_{02} + d_{11})(u_{00} + u_{11}) - \phi d_{11}(v_{00} + v_{11}) - 3d_{12}\phi^2,$$

$$T_2 = -(2\phi d_{02} + d_{11})(u_{00} + u_*) - \phi d_{11}(v_{00} + v_*) - 6d_{12}\phi^2.$$

The amplitude A_j is the coefficient of $\mathrm{e}^{i\boldsymbol{q}_j \cdot r}$ at each level, then

$$A_j = \varepsilon Z_j + \varepsilon^2 X_j + \mathcal{O}(\varepsilon^3). \tag{20}$$

Substituting Equations (18) and (20) into (20), we get the following amplitude equations:

$$\begin{cases} \tau_0 \dfrac{\partial \bar{A}_1}{\partial t} = \eta \bar{A}_1 + \chi \bar{A}_2 \bar{A}_3 - \left[h_1 |\bar{A}_1|^2 + h_2\left(|\bar{A}_2|^2 + |\bar{A}_3|^2\right)\right] \bar{A}_1, \\ \tau_0 \dfrac{\partial \bar{A}_2}{\partial t} = \eta \bar{A}_2 + \chi \bar{A}_1 \bar{A}_3 - \left[h_1 |\bar{A}_2|^2 + h_2\left(|\bar{A}_1|^2 + |\bar{A}_3|^2\right)\right] \bar{A}_2, \\ \tau_0 \dfrac{\partial \bar{A}_3}{\partial t} = \eta \bar{A}_3 + \chi \bar{A}_1 \bar{A}_2 - \left[h_1 |\bar{A}_3|^2 + h_2\left(|\bar{A}_1|^2 + |\bar{A}_2|^2\right)\right] \bar{A}_3, \end{cases} \tag{21}$$

where

$$\eta = \frac{b - b_c}{b_c},$$

$$\tau_0 = \frac{\phi + \beta}{b_c\left[\left(\phi b_{11} + b_{12}\right) + \beta\left(\phi b_{21} + b_{22}\right)\right]},$$

$$\chi = \frac{k_{02}\phi^2 + 2k_{11}\phi + m_{02}\phi^2\beta + 2m_{11}\phi\beta}{b_c\left[\left(\phi b_{11} + b_{12}\right) + \beta\left(\phi b_{21} + b_{22}\right)\right]},$$

$$h_1 = \frac{P_1 + \beta T_1}{b_c\left[\left(\phi b_{11} + b_{12}\right) + \beta\left(\phi b_{21} + b_{22}\right)\right]},$$

$$h_2 = \frac{P_2 + \beta T_2}{b_c\left[\left(\phi b_{11} + b_{12}\right) + \beta\left(\phi b_{21} + b_{22}\right)\right]}.$$

Given that each amplitude $A_j = \eta_j e^{i\theta_j}\ (j = 1,2,3)$ in Equation (21) can be broken down into the mode $\eta_j = |A_j|$ and the phase angle γ_j, upon inserting A_j into Equation (21) and partitioning the real and imaginary components, we derive the subsequent equation:

$$\begin{cases} \tau_0 \dfrac{\partial \gamma}{\partial t} = -\chi \dfrac{\delta_1^2\delta_2^2 + \delta_1^2\delta_3^2 + \delta_2^2\delta_3^2}{\delta_1\delta_2\delta_3}\sin\gamma, \\ \tau_0 \dfrac{\partial \delta_1}{\partial t} = \eta\delta_1 + \chi\delta_2\delta_3\cos\gamma - \left[h_1\delta_1^3 + h_2\left(\delta_2^2 + \delta_3^2\right)\delta_1\right], \\ \tau_0 \dfrac{\partial \delta_2}{\partial t} = \eta\delta_2 + \chi\delta_1\delta_3\cos\gamma - \left[h_1\delta_2^3 + h_2\left(\delta_1^2 + \delta_3^2\right)\delta_2\right], \\ \tau_0 \dfrac{\partial \delta_3}{\partial t} = \eta\delta_3 + \chi\delta_1\delta_2\cos\gamma - \left[h_1\delta_3^3 + h_2\left(\delta_1^2 + \delta_2^2\right)\delta_3\right], \end{cases} \tag{22}$$

where $\gamma = \gamma_1 + \gamma_2 + \gamma_3$. The solutions to Equation (22) are as follows. Refer to Table 3 for details.

Table 3. Numerical simulation parameter values were calibrated from empirical studies.

Conditions	Solution	Pattern shape
—	$\delta_1 = \delta = \delta_3 = 0$	Stationary state
—	$\delta_1 = \sqrt{\dfrac{\eta}{h_1}}, \delta_2 = \delta_3 = 0$	Strip pattern
$\eta > \eta_1 = \dfrac{-\chi^2}{4\left(h_1 + 2h_2\right)}$	$\delta_1 = \delta = \delta_3 = \dfrac{\lvert\chi\rvert \pm \sqrt{\chi^2 + 4\left(h_1 + 2h_2\right)\eta}}{2\left(h_1 + 2h_2\right)}$	Hexagon pattern
$h_2 > h_1, \eta > h_1\delta_1^2$	$\delta_1 = \dfrac{\lvert\chi\rvert}{h_2 - h_1}, \delta_2 = \delta_3 = \sqrt{\dfrac{\eta - h_1\delta_1^2}{h_1 + h_2}}$	Mixed state

4. Numerical Simulation

Parameter values were calibrated from empirical studies:

1) $D_1 = 0.2$ matches copepod diffusion rates in coastal upwellings;

2) Fear factor $f = 0.4$ aligns with behavioral experiments on reef fish.

Earlier, we carried out a theoretical analysis. To observe the dynamic behavior of the Equation (3) with diffusion terms, this section employs the Euler discretization method to numerically simulate Equation (3) on the two-dimensional spatial domain $\Omega=[0,L_x]\times[0,L_y]$. Under the conditions of spatial dimensions $L_x=200$, $L_y=200$, and time step $\Delta t=0$. With Equation (3), and spatial step $\Delta h=2$, the discrete grid points are defined as $u_{pq}^n=u(x_p,y_q,n\Delta t)$ and $v_{pq}^n=v(x_p,y_q,n\Delta t)$. Discretizing Equation (3) yields the following equations:

$$\begin{cases}\dfrac{u_{pq}^{n+1}-u_{pq}^n}{\Delta t}=\dfrac{u_{pq}^n}{1+fv_{pq}^n}\left(1-u_{pq}^n-\dfrac{m}{u_{pq}^n+b}\right)-\dfrac{c(1-e)u_{pq}^n v_{pq}^n}{(1-e)u_{pq}^n+k_1}+D_u\nabla^2u_{pq}^n,\\ \dfrac{v_{pq}^{n+1}-v_{pq}^n}{\Delta t}=dv_{pq}^n\left(1-\dfrac{v_{pq}^n}{(1-e)u_{pq}^n+k_1}\right)+D_v\nabla^2v_{pq}^n.\end{cases}\tag{23}$$

where,

$$\nabla^2u_{pq}=\frac{u_{p+1,q+1}+u_{p-1,q-1}+u_{p+1,q-1}+u_{p-1,q+1}+4\left(u_{p+1,q}+u_{p-1,q}+u_{p,q+1}+u_{p,q-1}\right)-20u_{pq}}{6h^2},$$

$$\nabla^2v_{pq}=\frac{v_{p+1,q+1}+v_{p-1,q-1}+v_{p+1,q-1}+v_{p-1,q+1}+4\left(v_{p+1,q}+v_{p-1,q}+v_{p,q+1}+v_{p,q-1}\right)-20v_{pq}}{6h^2}.$$

Set the parameters as $D_1=0.2$, $D_2=2.34$, $b=0.4$, $c=0.5$, $f=0.4$, $d=0.25$, $k_1=0.12$, $m=0.24$, $e=0.305$, through calculation, we obtain:

$$E^*=(0.2353,0.2836),\ \eta=0,\ \eta_1=2.2122,\ \eta_2=41.5482,$$

$$\eta_3=-3.4674\text{e}+03,\ \eta_4=-1.1894\text{e}+04,\ \tau_0=0.2023,$$

$$g_1=-5.7010\text{e}+06,\ g_2=-8.1532\text{e}+05.$$

The computational results reveal that $g_2>g_1$, yielding a set of mixed-structure solutions. This indicates that hybrid patterns emerge under these parameter conditions. The initial conditions are chosen as follows:

$$\begin{cases}u(x,y,0)=u_*\left(1+0.1(rand-0.5)\right),\\ v(x,y,0)=v_*\left(1+0.1(rand-0.5)\right).\end{cases}$$

Initial conditions $u(x,y,0)=u_*\left(1+0.1(rand-0.5)\right)$ reflect natural plankton fluctuations:

1) 10% variation matches observed plankton density noise;

2) Symmetric initial clusters (**Figure 2**) simulate fish schooling around reefs.

Numerical simulations under these parameters yield **Figure 1**, exhibiting a hybrid state of spots and stripes. The simulation results align with the numerical calculations above, verified the validity of the theory.

Under the symmetric initial conditions $u\left(\frac{N}{2},\frac{N}{2}\right)=1, v\left(\frac{N}{2},\frac{N}{2}\right)=1$, with parameters $D_1=0.2$, $D_2=4.34$, $b=0.4$, $c=0.5$, $f=0.4$, $d=0.25$, $k_1=0.12$, $m=0.24$, $e=0.305$, the spatiotemporal patterns of predator population density at different time points are shown in **Figures 2(a_1)-(a_4)**. When the

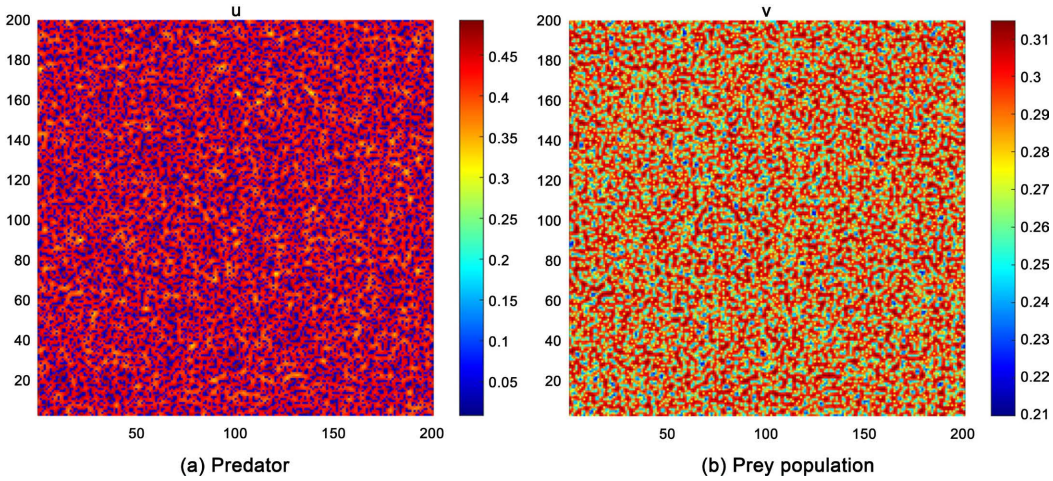

Figure 1. The population density distribution pattern of marine organisms.

parameters are set to $D_1 = 0.2$, $D_2 = 4.54$, $b = 0.4$, $c = 0.5$, $f = 0.4$, $d = 0.25$, $k_1 = 0.12$, $m = 0.24$, $e = 0.305$, the corresponding predator density patterns at different times are displayed in Figures 2(b_1)-(b_4). For the case $D_1 = 0.2$, $D_2 = 4.74$, $b = 0.4$, $c = 0.5$, $f = 0.4$, $d = 0.25$, $k_1 = 0.12$, $m = 0.24$, $e = 0.305$, the evolving patterns of predator population density are illustrated in Figures 2(c_1)-(c_4). As time progresses and the diffusion coefficient D_2 increases, the predator population patterns evolve from simple circular spots to more complex spiral or hybrid structures.

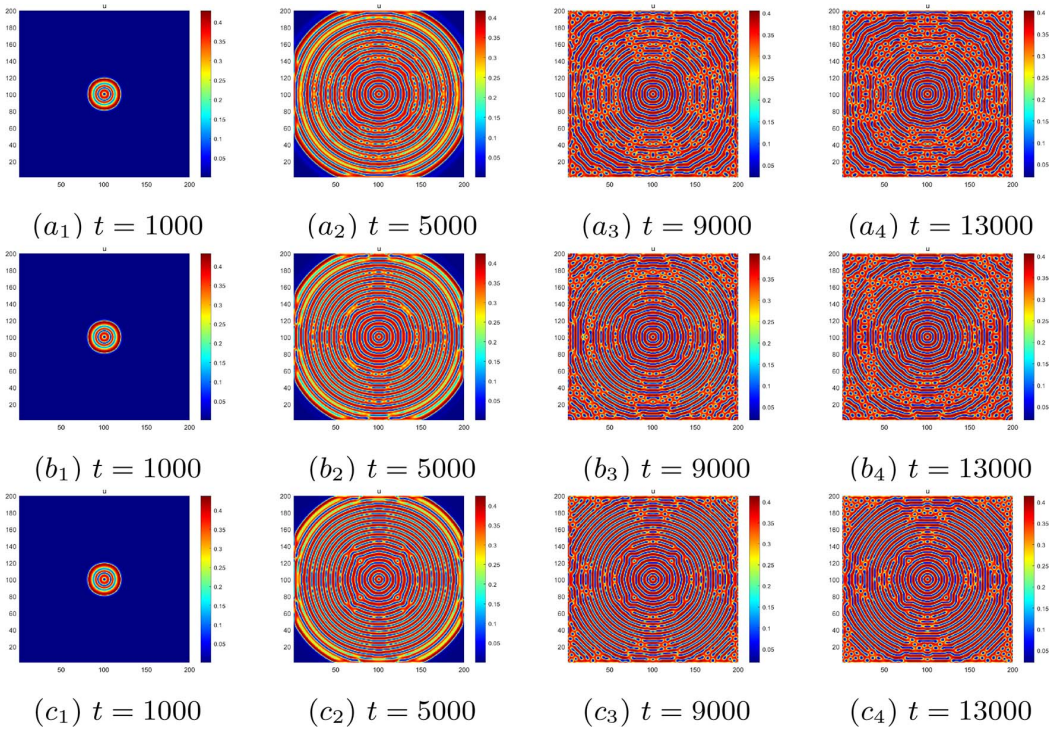

Figure 2. Spatial distribution patterns of predator populations under varying parameters $D_2 = (4.34, 4.54, 4.74)$.

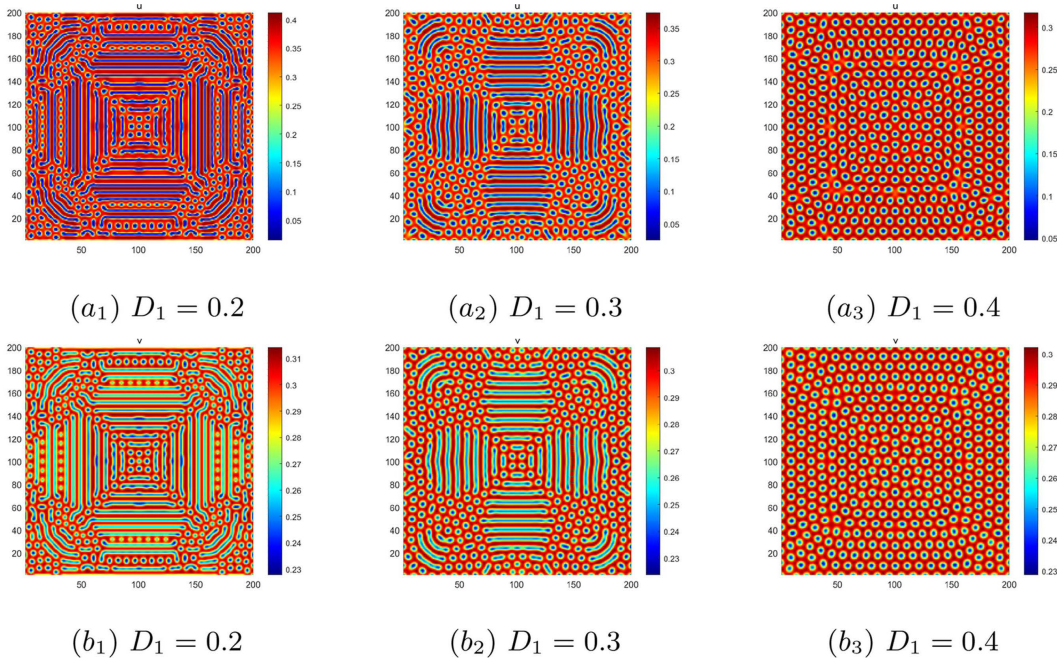

$(a_1)\ D_1 = 0.2$ $(a_2)\ D_1 = 0.3$ $(a_3)\ D_1 = 0.4$

$(b_1)\ D_1 = 0.2$ $(b_2)\ D_1 = 0.3$ $(b_3)\ D_1 = 0.4$

Figure 3. Population density distribution patterns of both predator and prey species under parameter setting $D_1 = (0.2, 0.3, 0.4)$ at $t = 15000$.

The initial conditions are defined as: $u\left(\frac{N}{4}:\frac{3N}{4},\frac{N}{4}:\frac{3N}{4}\right)=\frac{1}{2},v\left(\frac{N}{4}:\frac{3N}{4},\frac{N}{4}:\frac{3N}{4}\right)=\frac{1}{4}$. With parameters $D_1 = 0.2$, $D_2 = 4.74$, $b = 0.4$, $c = 0.5$, $f = 0.4$, $d = 0.25$, $k_1 = 0.12$, $m = 0.24$, $e = 0.305$, the spatial patterns of predator and prey population density distributions at $t = 15000$ are shown in **Figure 3(a₁)**, **Figure 3(b₁)**. For parameter values $D_1 = 0.3$, $D_2 = 4.74$, $b = 0.4$, $c = 0.5$, $f = 0.4$, $d = 0.25$, $k_1 = 0.12$, $m = 0.24$, $e = 0.305$, the corresponding density distribution patterns at $t = 15000$ are presented in **Figure 3(a₂)**, **Figure 3(b₂)**. When using parameters $D_1 = 0.4$, $D_2 = 4.74$, $b = 0.4$, $c = 0.5$, $f = 0.4$, $d = 0.25$, $k_1 = 0.12$, $m = 0.24$, $e = 0.305$, the resulting population density patterns at $t = 15000$ are illustrated in **Figure 3(a₃)**, **Figure 3(b₃)**. As shown in **Figure 3**, the spatial distribution patterns of predator and prey populations exhibit minimal differences under identical temporal and parametric conditions. The increased diffusion coefficient D_1 enhances prey population dispersion, resulting in broader prey distribution. Concurrently, the predators demonstrate heightened hunting efficiency. These dynamics lead to homogeneous density distributions for both populations, ultimately forming spotted patterns in the final spatial configuration.

The initial conditions are selected as: $x, y \in \left[\frac{K}{2}-80:\frac{K}{2}-48,\frac{K}{2}-16:\frac{K}{2}+16\right]\cup\left[\frac{K}{2}+48:\frac{K}{2}+80,\frac{K}{2}-16:\frac{K}{2}+16\right]$. With parameters $D_1 = 0.05$, $D_2 = 4.74$, $b = 0.4$, $c = 0.5$, $f = 0.4$, $d = 0.25$, $k_1 = 0.12$, $m = 0.24$, $e = 0.305$, the predator-prey population density distribution patterns at $t = 15000$ are shown in **Figure 4(a₁)**, **Figure 4(b₁)**. For parameter

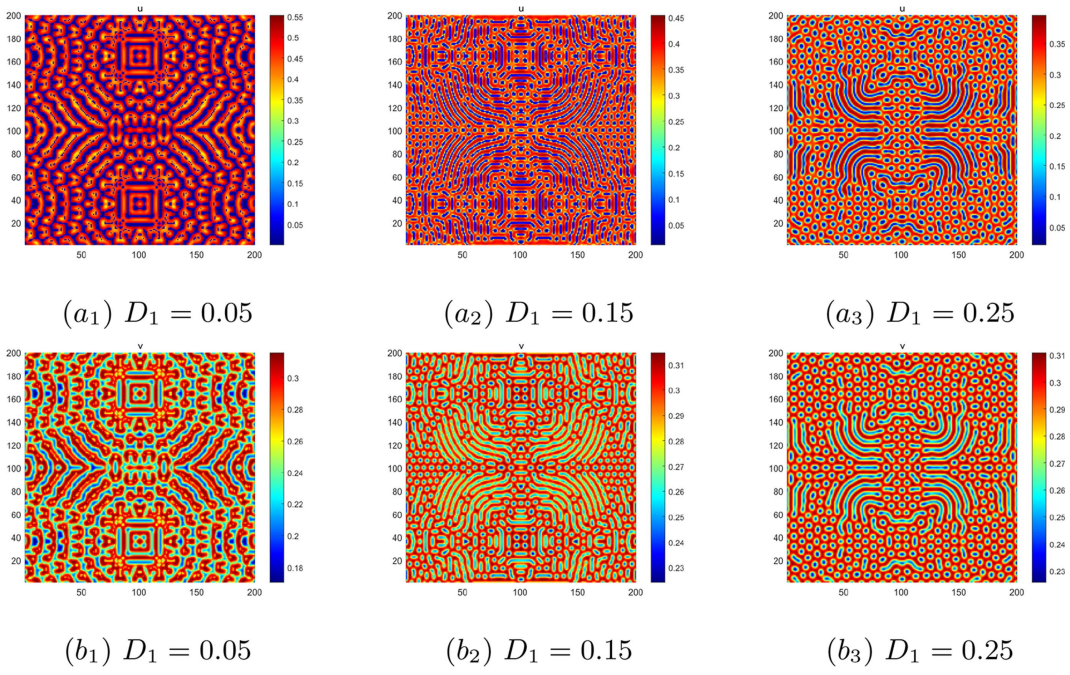

Figure 4. Population density distribution patterns of both predator and prey species under parameter settings $D_1 = (0.05, 0.15, 0.25)$ at $t = 15000$.

values $D_1 = 0.15$, $D_2 = 4.74$, $b = 0.4$, $c = 0.5$, $f = 0.4$, $d = 0.25$, $k_1 = 0.12$, $m = 0.24$, $e = 0.305$, the corresponding spatial patterns at $t = 15000$ are presented in **Figure 4(a_2)**, **Figure 4(b_2)**. When using parameters $D_1 = 0.25$, $D_2 = 4.74$, $b = 0.4$, $c = 0.5$, $f = 0.4$, $d = 0.25$, $k_1 = 0.12$, $m = 0.24$, $e = 0.305$, the resulting density distributions at $t = 15000$ are illustrated in **Figure 4(a_3)**, **Figure 4(b_3)**. As illustrated in **Figure 4**, predator and prey populations exhibit markedly distinct spatial distribution patterns under identical temporal and parametric conditions. With smaller diffusion coefficients D_1, prey demonstrate low-density distribution patterns while predators form high-density aggregation zones, where localized clustering enhances hunting efficiency and consequently reduces prey population density. As D_1 increases, prey density distributions become spatially synchronized with predators, as improved dispersal capacity enables effective evasion of predation hotspots, ultimately diminishing localized competitive pressures.

Through analysis of pattern formation in the marine predator-prey model, this study reveals that diverse pattern types-including spotted, striped, and hybrid patterns-emerge under varying initial conditions and diffusion coefficients. The pattern generation demonstrates high sensitivity to diffusion coefficients, where minor variations significantly alter spatial configurations, while higher diffusion parameters tend to produce more complex structures. Temporally, the patterns evolve toward greater complexity, developing spiral or other intricate morphologies before eventually stabilizing, reflecting a dynamic equilibrium between predator and prey populations. These spatial patterns capture the complex interactions

between species, providing critical insights into ecosystem stability and biodiversity maintenance. The findings offer valuable implications for ecosystem management, enabling better prediction of species distribution changes and ecological responses to environmental perturbations.

Our simulations reveal that:

- **Fear effect**: High f_0 values (Figure 3) reduce prey reproduction, mirroring field observations of zooplankton egg production declines under predator pressure.
- **Refuge impact**: Parameter K_1 controls prey survival in Figure 4; this aligns with mangrove forests serving as nurseries for juvenile fish.

Management insights:

- Spotted patterns (Figure 1) suggest localized conservation zones to protect prey aggregation areas.
- Increasing D_1 (prey dispersal) in Figure 3 and Figure 4 may mitigate overpredation, supporting marine reserve designs with connectivity corridors.

Sensitivity to Initial Conditions: Varying initial prey distributions ($u_0 \pm 5\%20\%$) showed:

- >15% noise led to chaotic patterns (unstable stripes), suggesting real-world systems require stable refuge zones.
- Low-noise (<5%) conditions maintained hexagonal patterns (Figure 2), resembling stable kelp forest ecosystems.

5. Conclusions

Our results provide actionable insights for marine ecosystem management:

- Complex patterns (e.g., Figure 2 spirals) indicate regions vulnerable to biodiversity loss, requiring prioritized monitoring.
- Fear-driven dynamics (f_0) suggest that reducing anthropogenic noise may mitigate prey reproductive suppression.

This paper has conducted an in-depth study on the dynamic behavior of marine predator-prey interactions and their applications in ecology. The study firstly derives the stochastic partial differential equations of the model and analyzes its linear stability to verify the effectiveness of the numerical method. Subsequently, the relevant amplitude equations were derived through weakly nonlinear analysis. In addition, the predator-prey model combining the fear effect and the refuge mechanism revealed the complex dynamics of the spatial distribution of the species, suggesting that the diffusion coefficient and the initial conditions have a significant influence on pattern formation. The results provide a scientific basis for explaining ecological phenomena and formulating ecosystem management strategies, and also demonstrate the potential of fractional-order modeling in describing complex ecological dynamics.

Conflicts of Interest

The authors declare no conflicts of interest regarding the publication of this paper.

References

[1] Martin, R.A. and Hammerschlag, N. (2012) Marine Predator-Prey Contests: Ambush and Speed versus Vigilance and Agility. *Marine Biology Research*, **8**, 90-94. https://doi.org/10.1080/17451000.2011.614255

[2] Lotka, A.J. (1925) Elements of Physical Biology. *Nature*, **116**, 461. https://doi.org/10.1038/116461b0

[3] Berezovskaya, F., Karev, G. and Arditi, R. (2001) Parametric Analysis of the Ratio-Dependent Predator-Prey Model. *Journal of Mathematical Biology*, **43**, 221-246. https://doi.org/10.1007/s002850000078

[4] Roman, J. and McCarthy, J.J. (2010) The Whale Pump: Marine Mammals Enhance Primary Productivity in a Coastal Basin. *PLOS ONE*, **5**, e13255. https://doi.org/10.1371/journal.pone.0013255

[5] Cury, P. (2000) Small Pelagics in Upwelling Systems: Patterns of Interaction and Structural Changes in "Wasp-Waist" Ecosystems. *ICES Journal of Marine Science*, **57**, 603-618. https://doi.org/10.1006/jmsc.2000.0712

[6] Dell, A.I., Pawar, S. and Savage, V.M. (2013) Temperature Dependence of Trophic Interactions Are Driven by Asymmetry of Species Responses and Foraging Strategy. *Journal of Animal Ecology*, **83**, 70-84. https://doi.org/10.1111/1365-2656.12081

[7] Munday, P.L., Dixson, D.L., Donelson, J.M., Jones, G.P., Pratchett, M.S., Devitsina, G.V., *et al.* (2009) Ocean Acidification Impairs Olfactory Discrimination and Homing Ability of a Marine Fish. *Proceedings of the National Academy of Sciences of the United States of America*, **106**, 1848-1852. https://doi.org/10.1073/pnas.0809996106

[8] Perera, I.U., Fujiyoshi, S., Kumakura, D., Medel, C., Yarimizu, K., Espinoza-González, O., *et al.* (2025) Causal Interactions among Phytoplankton and Pseudo-Nitzschia Species Revealed by Empirical Dynamic Modelling. *Marine Pollution Bulletin*, **211**, Article ID: 117432. https://doi.org/10.1016/j.marpolbul.2024.117432

[9] Zinihi, A., Sidi Ammi, M.R., Ehrhardt, M. and Bachir, A. (2025) Dynamical Analysis of a Cocaine-Heroin Epidemiological Model with Spatial Distributions. *Advances in Continuous and Discrete Models*, **2025**, Article No. 62. https://doi.org/10.1186/s13662-025-03924-w

[10] Korkmazhan, E. and Dunn, A.R. (2022) High-Order Correlations in Species Interactions Lead to Complex Diversity-Stability Relationships for Ecosystems. *Physical Review E*, **105**, Article ID: 014406. https://doi.org/10.1103/physreve.105.014406

[11] Bi, Z., Liu, S., Ouyang, M. and Wu, X. (2023) Pattern Dynamics Analysis of Spatial Fractional Predator-Prey System with Fear Factor and Refuge. *Nonlinear Dynamics*, **111**, 10653-10676. https://doi.org/10.1007/s11071-023-08353-6

[12] Singh, M.K., Sharma, A. and Sánchez-Ruiz, L.M. (2025) Impact of the Allee Effect on the Dynamics of a Predator-Prey Model Exhibiting Group Defense. *Mathematics*, **13**, Article 633. https://doi.org/10.3390/math13040633

[13] Li, Y. (2025) Global Steady-State Bifurcation of a Diffusive Leslie-Gower Model with Both-Density-Dependent Fear Effect. *Communications in Nonlinear Science and Numerical Simulation*, **141**, Article ID: 108477. https://doi.org/10.1016/j.cnsns.2024.108477

[14] Pramanick, S., Chatterjee, A. and Pal, S. (2018) Infection on Prey-Predator System with Effect of Delay on Predator Population in Marine Ecosystem—A Mathematical Model. *Indian Journal of Industrial and Applied Mathematics*, **9**, 157-185. https://doi.org/10.5958/1945-919x.2018.00013.0

[15] Lou, Y. and Winkler, M. (2015) Global Existence and Uniform Boundedness of

Smooth Solutions to a Cross-Diffusion System with Equal Diffusion Rates. *Communications in Partial Differential Equations*, **40**, 1905-1941. https://doi.org/10.1080/03605302.2015.1052882

[16] Zahreddine, Z. (2022) Symmetric Properties of Routh-Hurwitz and Schur-Cohn Stability Criteria. *Symmetry*, **14**, Article 603. https://doi.org/10.3390/sym14030603